

Supporting Information:

Kinetic Monte Carlo Simulations of Sodium Ion

Transport in NaICON Electrodes

Ziliang Wang,[†] Tara Prasad Mishra,^{†,§} Weihang Xie,[†] Zeyu Deng,[†]
Gopalakrishnan Sai Gautam,[‡] Anthony K. Cheetham,^{†,||} and Pieremanuele
Canepa^{*,†,⊥}

[†]*Department of Materials Science and Engineering, National University of Singapore, 9
Engineering Drive 1, 117575, Singapore*

[‡]*Department of Materials Engineering, Indian Institute of Science, Bengaluru, Karnataka,
560012, India*

^{*}*Department of Chemical and Biomolecular Engineering, National University of Singapore,
4 Engineering Drive 4, 117585, Singapore*

[§]*Singapore-MIT Alliance for Research and Technology, 1 CREATE Way, 10-01 CREATE
Tower, Singapore 138602, Singapore*

^{||}*Materials Department and Materials Research Laboratory, University of California, Santa
Barbara 93106 California, USA*

[⊥]*Department of Electrical & Computer Engineering, University of Houston, Houston,
Texas, 77204, United States of America*

E-mail: pcanepa@nus.edu.sg, pcanepa@central.uh.edu

Contents

1	First-Principles Calculations of Migration Barriers	S-3
2	Local Cluster Expansion Formalism	S-20
3	Kinetic Monte Carlo Simualtions	S-27

1 First-Principles Calculations of Migration Barriers

Using the Vienna *Ab initio* Simulation Package (VASP),^{S1,S2} the spin-polarized first-principles calculations based on density functional theory (DFT) were performed to evaluate the Na⁺ migration activation energies within the NaSICON frameworks. Projected Augmented Wave (PAW) potentials^{S3} to deal with the core-electron wave functions were selected as Na 3s¹ 08Apr2002, P 3s²3p³ 06Sep2000, O 2s²2p⁴ 08Apr2002, V_pv 3p⁶3d⁴4s¹ 07Sep2000, Cr_pv 3p⁶3d⁵4s¹ 02Aug2007, and Ti_pv 3d³4s¹ 07Sep2000. The Strongly Constrained and Appropriately Normed (SCAN)^{S4} meta-Generalized Gradient Approximations (meta-GGA) functionals were employed to calculate the exchange-correlation energy. SCAN incorporates the kinetic energy density and has been proved to accurately provide the ground-state electronic structures,^{S5} and the migration energies.^{S6} The Hubbard *U* corrections of 1.0 eV for V, 0.0 eV for Cr, and 2.5 eV for Ti were used (SCAN + *U*) to improve the strong on-site localization of 3d electrons.^{S5,S7} A Γ -point-centered sampling mesh and 520 eV kinetic energy cut-off of the expansion of the valence-electron plane wave functions were applied to all structures, i.e., Na_xV₂(PO₄)₃ (N_xVP), Na_xCr₂(PO₄)₃ (N_xCP), and Na_xTi₂(PO₄)₃ (N_xTP).

The Na⁺ migration barriers were evaluated using Nudged Elastic Band (NEB) theory^{S8,S9} at the compositions of N₁VP, N₂VP, N₃VP and N₄VP of the N_xVP systems, through DFT implemented in VASP. For each composition, the initial structure was selected from the ground-state configurations from our previous works.^{S10,S11} Notably, the initial structures adopt the rhombohedral ($R\bar{3}c$) symmetry at x = 1, and 4, and monoclinic symmetry at x = 2 ($C2/c$), and 3 (Cc) before structural optimization. All structures were transformed to a pseudo-cubic cell with 8 formula units (f.u.). The transformation matrix for monoclinic to rhombohedral, and rhombohedral to pseudo-cubic is [[1, 0, 1], [-1, 1, 1], [0, -1, 1]], and [[1, 1, -1], [-1, 1, 1], [1, -1, 1]], respectively.

For the end members of N_xVP, where only Na(1) sites are occupied at N₁VP, and all Na(1) and Na(2) sites are occupied at N₄VP, we measured the Na⁺ migration pathways of

$\text{Na}(1)\text{-Na}(2)\text{-Na}(1)$, and $\text{Na}(1)\text{-Na}(2)$, respectively. At the composition of $x = 2$, and 3, we measured the path of $\text{Na}(2)\text{-Na}(1)\text{-Na}(2)$. Specifically, at the global minimum composition of N_3VP with partially occupied $\text{Na}(2)$ sites,^{S10} we enumerated all possible local Na/vacancy environments within a single migration unit (m.u.) (see main manuscript) by varying the number of inactive $\text{Na}(2)$ sites from 0 to 4 while keeping the global concentration of Na fixed. Subsequently, to approximate the various migration pathways in NaSICON, we constructed 2 Na^+ transport paths within a single migration unit (m.u.), i.e., one is a straight path, and the other is a curved path, with the classification of αS_β or αC_β . All the enumerated migration units for NEB at N_3VP were identified in **Figure S1**. In this terminology, α stands for the number of inactive (“background”) Na-ions ($\text{Na}(2)$) which are fixed aside the migration pathways within the m.u., S/C index is the straight/curved-type migration path, and β indexes the number of possible enumerations within the $\alpha\text{S}/\alpha\text{C}$ group. For example, in **Figure S1(e), (g), and (i)**, the straight $\text{Na}(2)\text{-Na}(1)\text{-Na}(2)$ pathways were constructed within a m.u. of 2 vacant $\text{Na}(2)$ sites (black circles) and 4 occupied $\text{Na}(2)$ sites (green & yellow circles), resulting in 2 $\text{Na}(2)$ sites (yellow circles) to be included in the migration path and 2 $\text{Na}(2)$ sites (green circles) fixed as “background” ions. In total, this 2S group consists of 3 possible enumerated pathways, thus they’re labeled as 2S_1, 2S_2, and 2S_3, as shown in **Figure S1(e), (g), and (i)**, respectively.

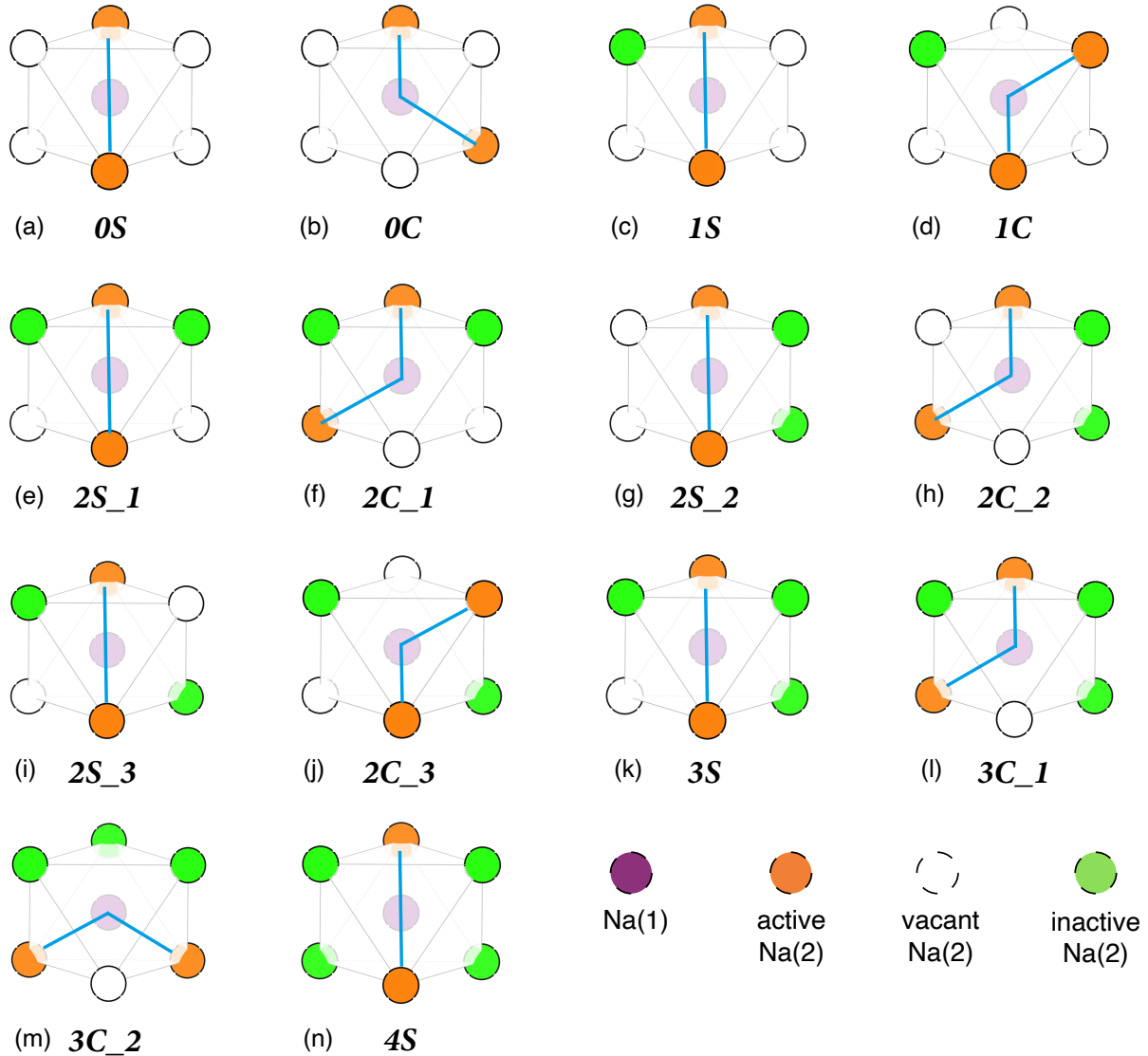


Figure S1: Migration units with varied Na/vacancy local environment at N₃VP to perform NEB. Migration pathways are identified by the blue solid lines. Centered Na(1), active Na(2) included in the diffusion pathways are shown with purple and yellow circles, respectively. Green circles denote the inactive Na(2) which are fixed as “background” ions while Na⁺ migrating, and the blank circles are the vacant Na sites. Notably, the Na⁺ diffusion pathways constructed for N₃TP and N₃CP follow the same migration unit configurations as shown here.

All the NEB migration barrier results computed for N₁VP, N₂VP, N₃VP, and N₄VP were summarized in **Figure S2**. **Table S1** contained all NEB results of Na_xV₂(PO₄)₃ corresponding to the hop events (i.e., Na(2)→Na(1) or Na(1)→Na(2)) along the migration pathways. Specifically, ΔE_{site} is the site energy difference between Na(2) and Na(1) ($E_{\text{Na@Na(2)}} - E_{\text{Na@Na(1)}}$), E_{KRA} is the Kinetically Resolved Activation Energy which is inde-

pendent of the direction of diffusion, and E_{barrier} is the migration barrier energy identified by the energy difference between the activated state and the most stable state of end points along the pathway.

All the calculated barriers are corresponding to 2 migration events, i.e., one is $\text{Na}(2) \rightarrow \text{Na}(1)$ and the other is $\text{Na}(1) \rightarrow \text{Na}(2)$ in all NEB at N₃VP, which enable us to average the two events to account for the complete migration energies within the specific migration unit. The E_{KRA} and the ΔE_{site} can be derived accordingly. In the case of fully sodiated structures (i.e., x = 4), we only considered the energies contributed from the half path of Na(1)-Na(2).

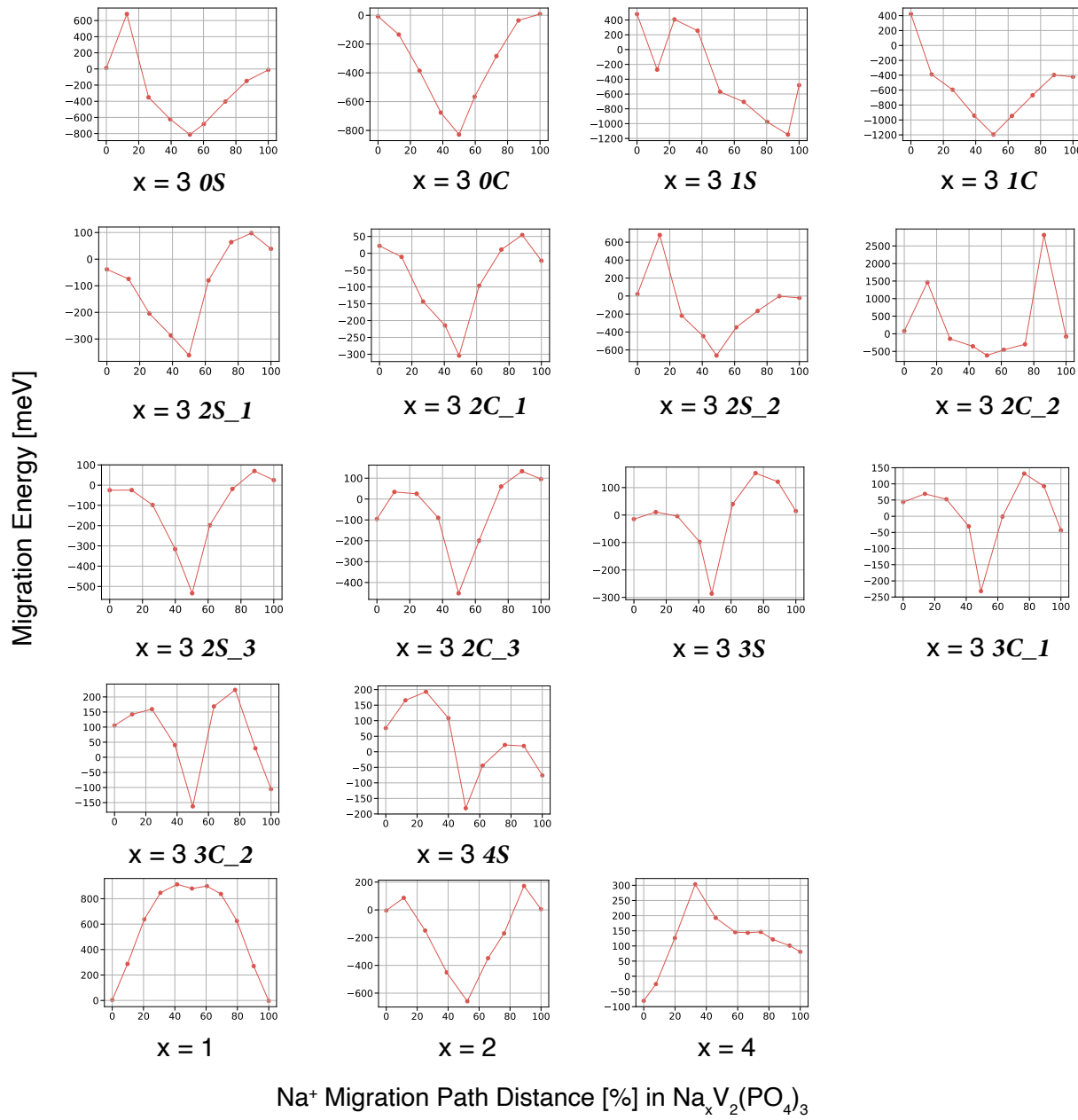


Figure S2: All migration barrier results of $\text{Na}_x\text{V}_2(\text{PO}_4)_3$ derived from NEB. For $x = 2$, and 3, the results are corresponding to the pathways between the 2 adjacent $\text{Na}(2)$ sites within a single migration unit via a center $\text{Na}(1)$ site (i.e., $\text{Na}(2)$ - $\text{Na}(1)$ - $\text{Na}(2)$ pathway), and the terminologies of all $x = 3$ pathways follow the description in **Figure S1**. For $x = 1$, the migration pathway is $\text{Na}(1)$ - $\text{Na}(2)$ - $\text{Na}(1)$, and $x = 4$ result is related to $\text{Na}(1)$ - $\text{Na}(2)$ pathway.

Table S1: Computed NEB results of ΔE_{site} , E_{KRA} , and E_{barrier} for $N_x\text{VP}$. All units are in meV. All results are corresponding to the hop events (Na(2)-Na(1)/Na(1)-Na(2)) as included in each migration pathway, as shown by the separate rows of each αS_β or αC_β group.

x in $N_x\text{VP}$		ΔE_{site}	E_{KRA}	E_{barrier}
x = 3	0S	823.9 801	1080.45 400.5	1492.4 801
	0C	821.1 837.5	410.55 418.75	821.1 837.5
	1S	960.7	480.35	960.7
	1C	1617.4 775.4	808.7 411.9	1617.4 799.6
	2S_1	322.5 399.6	161.25 258.9	322.5 458.7
	2C_1	326 281.6	163 217.3	326 358.1
	2S_2	326 281.6	163 217.3	326 358.1
	2C_2	695.5 537	1734.85 3159.8	2082.6 3428.3
	2S_3	509 558.8	254.8 324.5	509.3 603.9
	2C_3	355.7 547.5	307.85 311.25	485.7 585
	3S	271.5 300.9	161.35 288.65	297.1 439.1
	3C_1	275.6 188.2	163.3 269.8	301.1 363.9
	3C_2	268 57	188.1 357.5	322.1 386
	4S	257.5 105.4	245.95 150.8	374.7 203.5
x = 1		876.9 883.2	471.25 460.7	909.7 902.3
x = 2		653.8 662.8	418 499.1	744.9 830.5
x = 4		161.8	303.3	384.2

Figure S3 illustrates the on-site magnetic moments of V sites of $\text{Na}_3\text{V}_2(\text{PO}_4)_3$ in the case of **0S** (see **Figure S1a**), where the migrating Na^+ is surrounded by 4 vacancy sites, thus the local arrangement of V^{4+} states are observed.

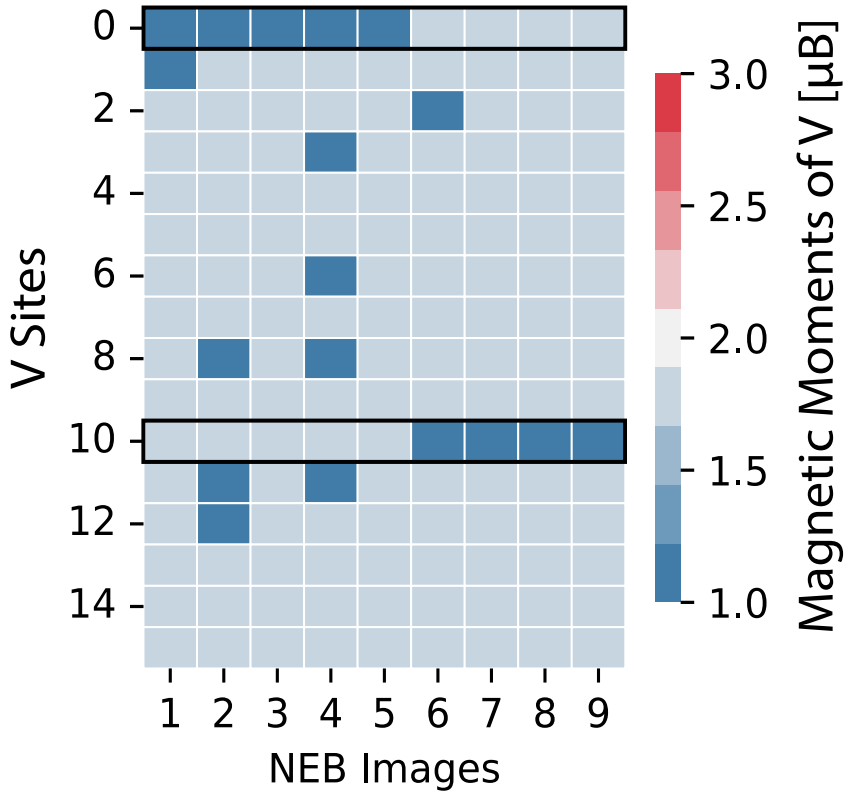


Figure S3: The on-site magnetic moments of V at N_3VP computed by NEB with SCAN + U framework. The row No. 0 and 10 specified with the black squares are the 2 V sites closest to the Na^+ migration pathway from $Na(2)$ (NEB Image1) to $Na(2)$ (NEB Image9), via the center $Na(1)$ (NEB Image4).

Similarly, we did NEB for all possible migration pathways of N_xCP and N_xTP systems, only at $x = 1, 3$, and 4 . The initial structures were selected from our previous work,^{S12} and further structurally optimized with SCAN + U framework. We enumerated the Na -vacancy local environment at $x = 3$ similar with **Figure S1** for N_xVP . To be noted, the ground-state structures at $x = 1, 3$, and 4 can be mapped with the same lattice symmetry among N_xCP , N_xTP , and N_xVP , and similar electrochemical cycling performance and phase behaviors among them has been reported.^{S10,S12-S16} All the NEB results for N_xCP and N_xTP are summarized in **Figures S4 & S5**, and **Tables S2 & S3**. To be noted, we exclude the results at N_4CP for generating its local cluster expansion formalism in order to avoid the complicated Jahn-Teller distortion caused by Cr^{2+} ($3d^4$), which could be accurately captured

by SCAN + U functional as shown in **Figure S6**.

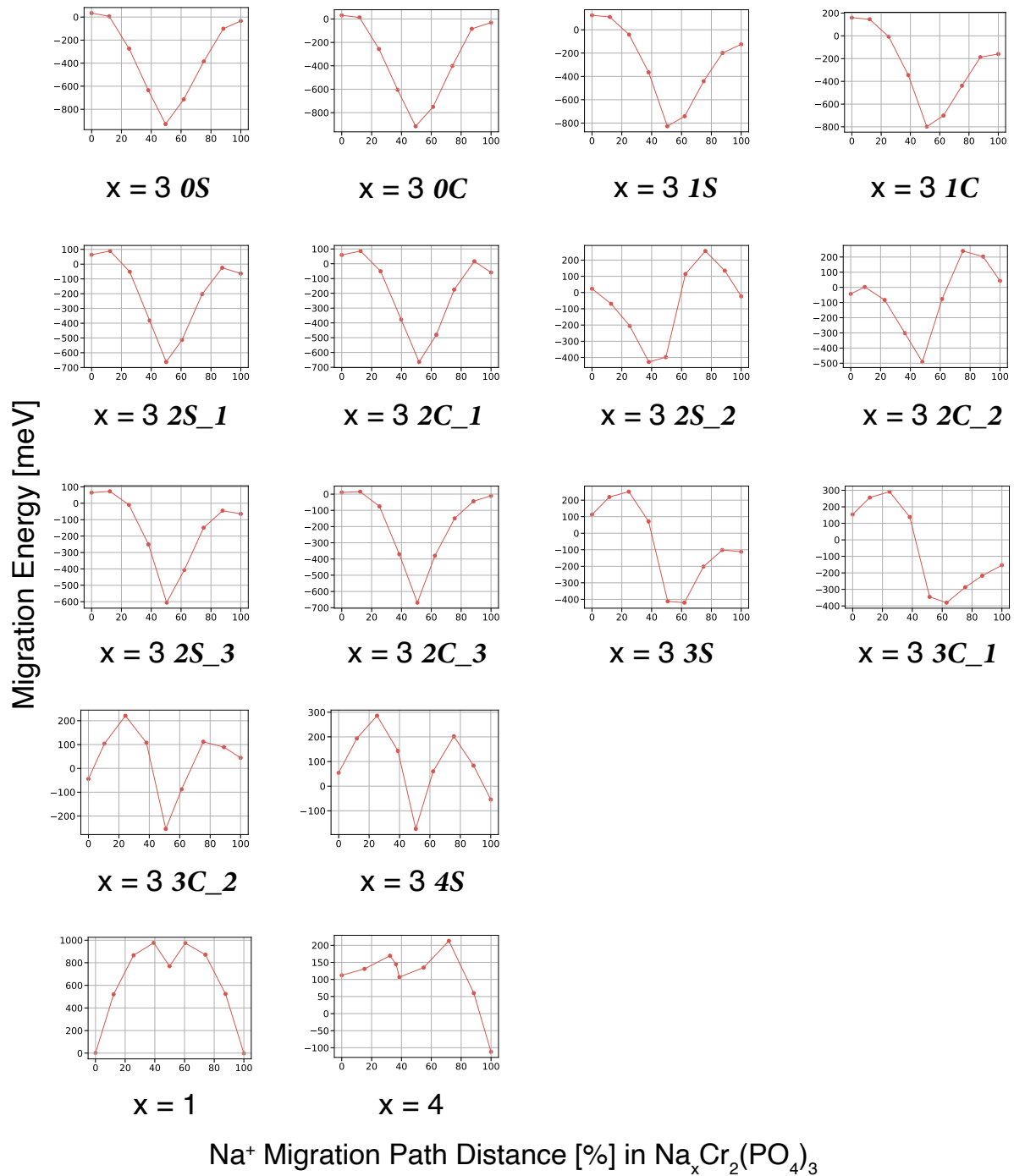


Figure S4: All migration barrier results of $\text{Na}_x\text{Cr}_2(\text{PO}_4)_3$ derived from NEB. For $x = 3$, the results are corresponding to the pathways between the 2 adjacent Na(2) sites within a single migration unit via a center Na(1) site (i.e., Na(2)-Na(1)-Na(2) pathway), and the terminologies of all $x = 3$ pathways follow the description for $N_x\text{VP}$ as in **Figure S1**. For $x = 1$, the migration pathway is Na(1)-Na(2)-Na(1), and $x = 4$ result is related to Na(1)-Na(2) pathway.

Table S2: Computed NEB results of ΔE_{site} , E_{KRA} , and E_{barrier} for $N_x\text{CP}$. All units are in meV. All results are corresponding to the hop events ($\text{Na}(2)\text{-Na}(1)/\text{Na}(1)\text{-Na}(2)$) included in each migration pathway, as shown by the separate rows of each αS_β or αC_β group.

x in $N_x\text{CP}$		ΔE_{site}	E_{KRA}	E_{barrier}
x = 3	0S	962.6 893.9	481.3 446.95	962.6 893.9
	0C	947.4 885	473.7 442.5	947.4 885
	1S	951.9 703.2	475.95 351.6	951.9 703.2
	1C	958.3 658.9	479.15 319.45	958.3 638.9
	2S_1	726.3 598.9	388.45 338.55	751.6 638
	2C_1	723.3 598.9	388.55 338.55	750.2 638
	2S_2	436.55 389.35	218.275 474.375	436.55 669.05
	2C_2	448.9 535.2	270.25 464.4	494.7 732
	2S_3	670.5 540.9	343.05 290.05	678.3 560.5
	2C_3	679.3 658.8	344.25 329.4	683.9 658.8
	3S	528.25 303.85	403.125 162.425	667.25 314.35
	3C_1	516.8 209.4	396.3 104.7	654.7 209.4
	3C_2	209.6 298.3	370 216.55	474.8 365.7
	4S	227.6 119.4	345.7 316	459.5 375.7
	x = 1	767.2 770.9	590.9 590.65	974.5 976.1
x = 4		224	213.1	325.1

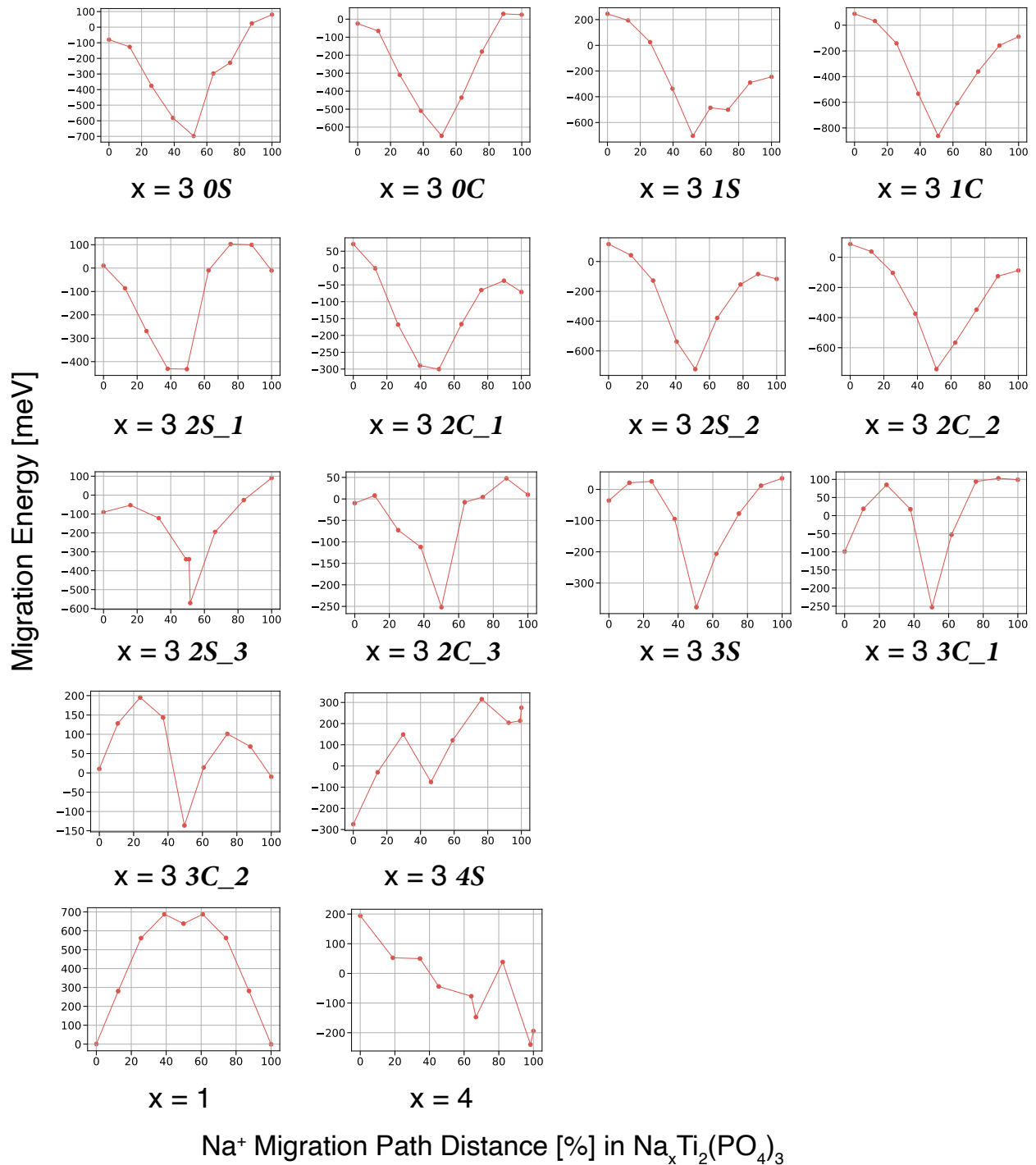


Figure S5: All migration barrier results of $\text{Na}_x\text{Ti}_2(\text{PO}_4)_3$ derived from NEB. For $x = 3$, the results are corresponding to the pathways between the 2 adjacent Na(2) sites within a single migration unit via a center Na(1) site (i.e., Na(2)-Na(1)-Na(2) pathway), and the terminologies of all $x = 3$ pathways follow the description for $\text{Na}_x\text{V}_2(\text{PO}_4)_3$ as in **Figure S1**. For $x = 1$, the migration pathway is Na(1)-Na(2)-Na(1), and $x = 4$ result is related to Na(1)-Na(2) pathway.

Table S3: Computed NEB results of ΔE_{site} , E_{KRA} , and E_{barrier} for $N_x \text{TP}$. All units are in meV. All results are corresponding to the hop events (Na(2)-Na(1)/Na(1)-Na(2)) included in each migration pathway, as shown by the separate rows of each αS_β or αC_β group.

x in $N_x \text{TP}$		ΔE_{site}	E_{KRA}	E_{barrier}
$x = 3$	$0S$	617.7 778.2	308.85 389.1	617.7 778.2
	$0C$	624.1 673.4	312.05 341.5	624.1 678.2
	$1S$	949.4 459.3	474.7 229.65	949.4 459.3
	$1C$	950.2 773.1	475.1 386.55	950.2 773.1
	$2S_1$	441.95 420.95	220.975 323.475	441.95 533.95
	$2C_1$	371.3 229.2	185.65 148	371.3 262.6
	$2S_2$	839.4 605.4	419.7 335.7	839.4 638.4
	$2C_2$	829.9 654.8	414.95 327.4	829.9 654.8
	$2S_3$	480.6 661.4	277.2 330.7	517.5 661.4
	$2C_3$	242.1 261.9	138.75 168.95	259.8 299.9
	$3S$	341.7 412.8	232.15 206.4	403 412.8
	$3C_1$	153.6 351.5	260.7 179.75	337.5 355.5
	$3C_2$	146.5 126.2	258.35 174.2	331.6 237.3
	$4S$	-297.85 252.15	274.975 166.675	423.9 292.75
$x = 1$		637.3 638.8	368.75 369.4	687.4 688.8
$x = 4$		388.8	194.4	388.8

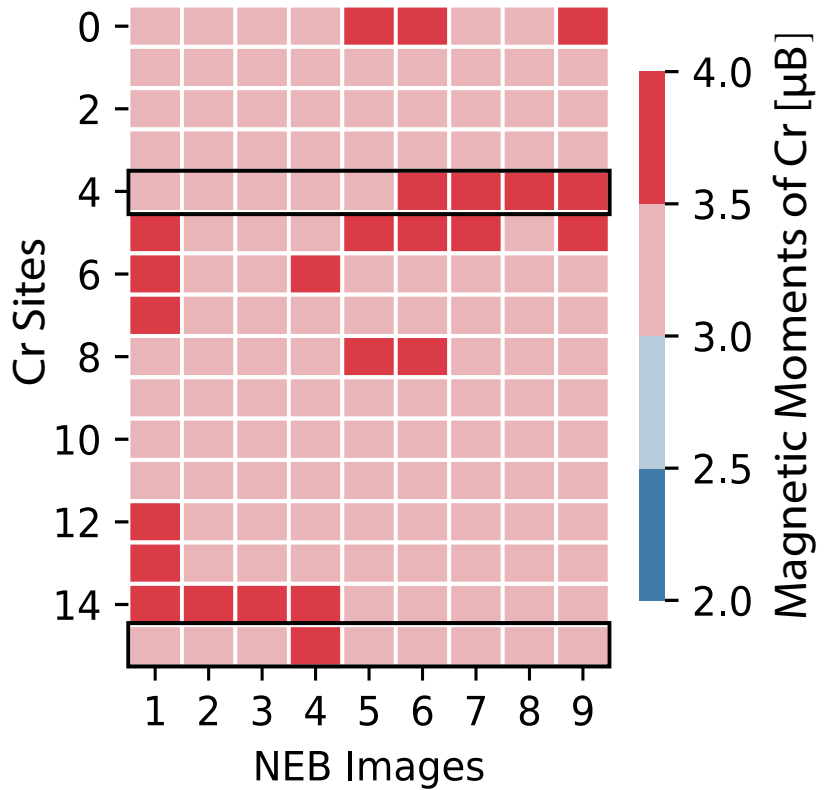


Figure S6: The on-site magnetic moments of Cr at N₄CP computed by NEB with SCAN + U framework. The row No. 4 and 15 specified with the black squares are the 2 Cr sites closest to the Na⁺ migration pathway from Na(2) (NEB Image1) to Na(1) (NEB Image9). Specifically, the distance between Cr site No.4 and the migrating Na⁺ decreased from 5.2 Å to 3.1 Å while Na⁺ diffused from Na(2) to Na(1).

Figure S7 plots the on-site magnetic moments of Ti, V, and Cr at $x = 1$. It's clear that although the tetra-valent state was observed for all three NaSICONs, the occupation of the 3d orbitals of them were different. The 3d electronic configurations was 3d⁰ for Ti^{IV}, 3d¹ for V^{IV}, and 3d² for Cr^{IV}. Regarding the on-site magnetic moments, all the Ti sites in Na₁Ti₂(PO₄)₃ exhibited 0.0 μ_B , all the V sites in Na₁V₂(PO₄)₃ exhibited 1.0 μ_B , and all the Cr sites in Na₁Cr₂(PO₄)₃ exhibited 2.1 μ_B , respectively.

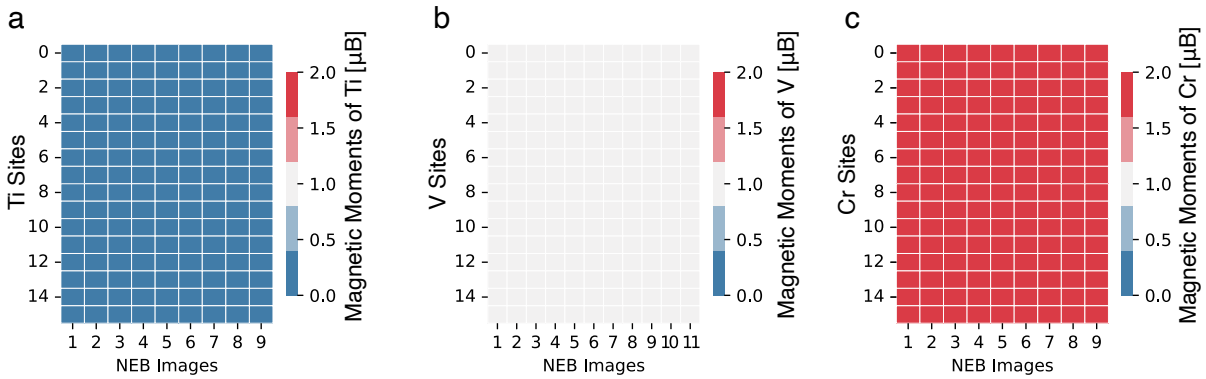


Figure S7: The on-site magnetic moments of Ti, V, and Cr at $x = 1$ of $\text{Na}_x\text{M}_2(\text{PO}_4)_3$ computed by NEB with SCAN + U framework.

Figure S8 plots the on-site magnetic moments of Ti, V, and Cr at $x = 3$. The major 3d electronic configurations was $3d^1$ for Ti^{III} , $3d^2$ for V^{III} , and $3d^3$ for Cr^{III} . Regarding the on-site magnetic moments, most of the Ti sites in $\text{Na}_3\text{Ti}_2(\text{PO}_4)_3$ exhibited $0.9 \mu_B$, and the Ti sites near the migrating Na-ion exhibited $0.0 \mu_B$. Most of the V sites in $\text{Na}_3\text{V}_2(\text{PO}_4)_3$ showed $1.8 \mu_B$, and the V sites near the migrating Na-ion showed $1.1 \mu_B$. Most of the Cr sites in $\text{Na}_3\text{Cr}_2(\text{PO}_4)_3$ exhibited $2.8 \mu_B$, and the Cr sites near the migrating Na-ion showed $2.4 \mu_B$.

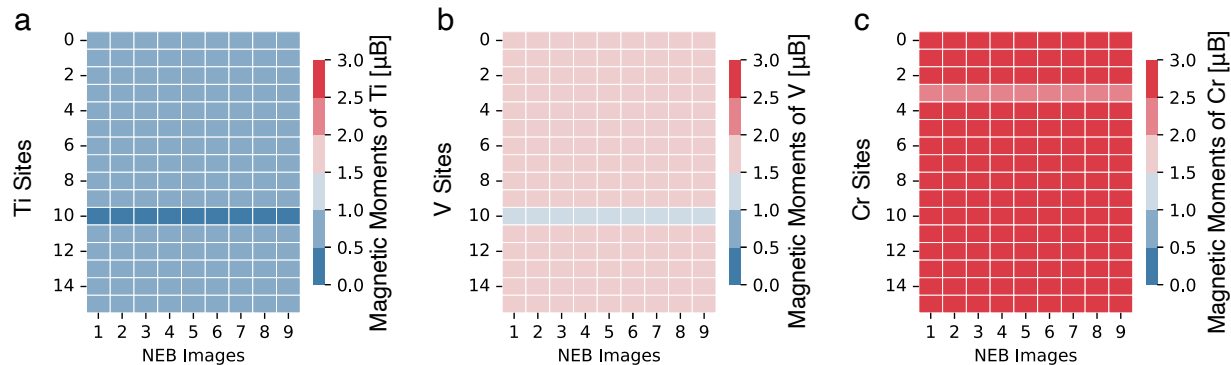


Figure S8: The on-site magnetic moments of Ti, V, and Cr at $x = 3$ of $\text{Na}_x\text{M}_2(\text{PO}_4)_3$ computed by NEB with SCAN + U framework.

For the further NEB performed for the NaSICONs with mixed transition metal elements, i.e., $\text{Na}_1\text{TiV}(\text{PO}_4)_3$, $\text{Na}_1\text{VCr}(\text{PO}_4)_3$, and $\text{Na}_1\text{TiCr}(\text{PO}_4)_3$, **Figure S9** shows the computed

magnetic moments of Ti & V at $\text{Na}_1\text{TiV}(\text{PO}_4)_3$, V & Cr at $\text{Na}_1\text{VCr}(\text{PO}_4)_3$, and V & Cr at $\text{Na}_1\text{TiCr}(\text{PO}_4)_3$. Note that the V^{V} oxidation states were observed at V sites No. 10 and 12 in panel a, which correspond to the closest V sites to the Na^+ migration pathway. The $\text{Cr}^{\sim\text{V}}$ oxidation states were observed at Cr sites No. 10 and 14 in panel c, which correspond to the closest Cr sites to the Na^+ migration pathway. Regarding the on-site magnetic moments, all the Ti sites in $\text{Na}_1\text{TiV}(\text{PO}_4)_3$ exhibited $0.0 \mu_B$, most of the V sites in $\text{Na}_1\text{TiV}(\text{PO}_4)_3$ exhibited $1.0 \mu_B$, and the V sites near the migrating Na-ion exhibited $0.0 \mu_B$. All the V and Cr sites in $\text{Na}_1\text{VCr}(\text{PO}_4)_3$ showed $0.1 \mu_B$, and $2.7 \mu_B$, respectively. All the Ti sites in $\text{Na}_1\text{TiCr}(\text{PO}_4)_3$ showed $0.0 \mu_B$, most of the Cr sites in $\text{Na}_1\text{TiCr}(\text{PO}_4)_3$ exhibited $1.9 \mu_B$, and the Cr sites near the migrating Na-ion exhibited $1.4 \mu_B$.

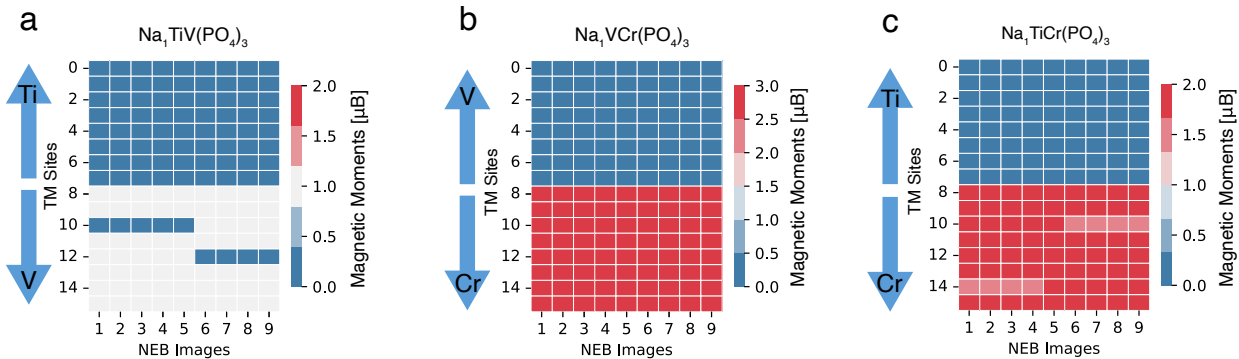


Figure S9: The on-site magnetic moments of Ti & V at $\text{Na}_1\text{TiV}(\text{PO}_4)_3$, V & Cr at $\text{Na}_1\text{VCr}(\text{PO}_4)_3$, and Ti & Cr at $\text{Na}_1\text{TiCr}(\text{PO}_4)_3$ computed by NEB with SCAN + U framework.

The corresponding minimum energy path of $\text{Na}(1) \rightarrow \text{Na}(2) \rightarrow \text{Na}(1)$ pathway for $\text{Na}_1\text{TiV}(\text{PO}_4)_3$, $\text{Na}_1\text{VCr}(\text{PO}_4)_3$, and $\text{Na}_1\text{TiCr}(\text{PO}_4)_3$ are shown in **Figure S10**. For $\text{Na}_1\text{TiV}(\text{PO}_4)_3$, we observed migration barrier of ~ 794 meV, and site energy difference between $\text{Na}(2)$ and $\text{Na}(1)$ of ~ 744 meV. For $\text{Na}_1\text{VCr}(\text{PO}_4)_3$, we observed migration barrier of ~ 613 meV, and site energy difference between $\text{Na}(2)$ and $\text{Na}(1)$ of ~ 576 meV. For $\text{Na}_1\text{TiCr}(\text{PO}_4)_3$, we observed migration barrier of ~ 774 meV, and site energy difference between $\text{Na}(2)$ and $\text{Na}(1)$ of ~ 650 meV.

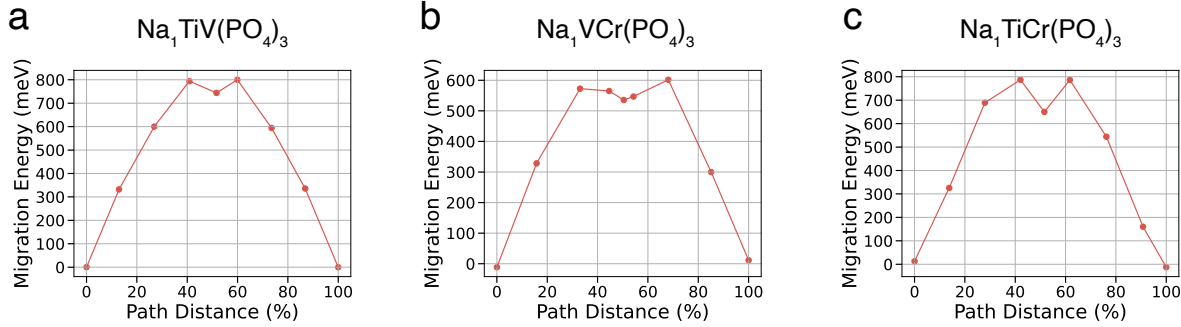


Figure S10: The computed minimum energy path of $\text{Na}_1\text{TiV}(\text{PO}_4)_3$ (panel a), $\text{Na}_1\text{VCr}(\text{PO}_4)_3$ (panel b), and $\text{Na}_1\text{TiCr}(\text{PO}_4)_3$ (panel c) by NEB with SCAN + U framework.

Figure S11 shows the computed magnetic moments of Ti & V at $\text{Na}_3\text{TiV}(\text{PO}_4)_3$, V & Cr at $\text{Na}_3\text{VCr}(\text{PO}_4)_3$, and V & Cr at $\text{Na}_3\text{TiCr}(\text{PO}_4)_3$. For all these three mixed-TM NaSICONs at Na_3 composition, only Ti^{III} , V^{III} and Cr^{III} oxidation states were found to serve as local charge arrangements for migrating Na^+ . Regarding the on-site magnetic moments, all the Ti and V sites in $\text{Na}_3\text{TiV}(\text{PO}_4)_3$ exhibited $0.9 \mu_B$, and $1.8 \mu_B$, respectively. All the V and Cr sites in $\text{Na}_3\text{VCr}(\text{PO}_4)_3$ exhibited $1.8 \mu_B$, and $2.8 \mu_B$, respectively. All the Ti and Cr sites in $\text{Na}_3\text{TiCr}(\text{PO}_4)_3$ exhibited $0.9 \mu_B$, and $2.8 \mu_B$, respectively.

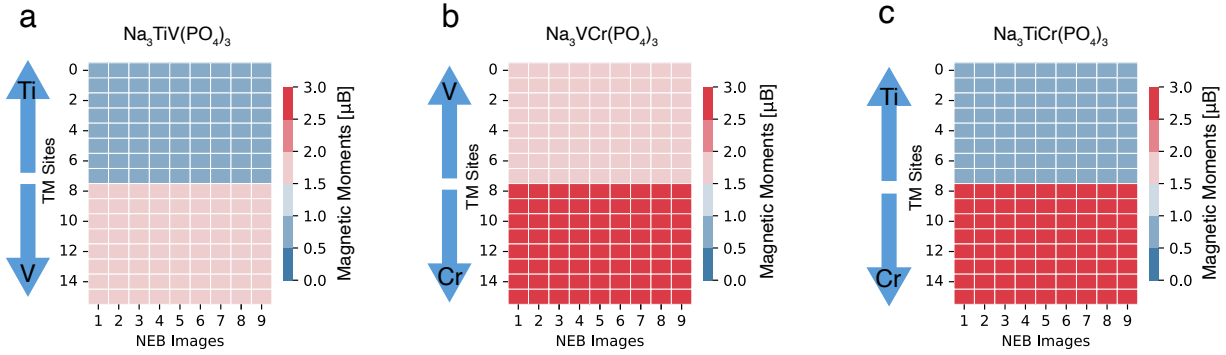


Figure S11: The on-site magnetic moments of Ti & V at $\text{Na}_3\text{TiV}(\text{PO}_4)_3$, V & Cr at $\text{Na}_3\text{VCr}(\text{PO}_4)_3$, and Ti & Cr at $\text{Na}_3\text{TiCr}(\text{PO}_4)_3$ computed by NEB with SCAN + U framework.

The corresponding computed minimum energy path for $\text{Na}_3\text{TiV}(\text{PO}_4)_3$, $\text{Na}_3\text{VCr}(\text{PO}_4)_3$, and $\text{Na}_3\text{TiCr}(\text{PO}_4)_3$ are shown in **Figure S12**. For $\text{Na}_3\text{TiV}(\text{PO}_4)_3$, we observed migration barrier of ~ 676 meV. For $\text{Na}_3\text{VCr}(\text{PO}_4)_3$, we observed migration barrier of ~ 719 meV. For $\text{Na}_3\text{TiCr}(\text{PO}_4)_3$, we observed migration barrier of ~ 667 meV.

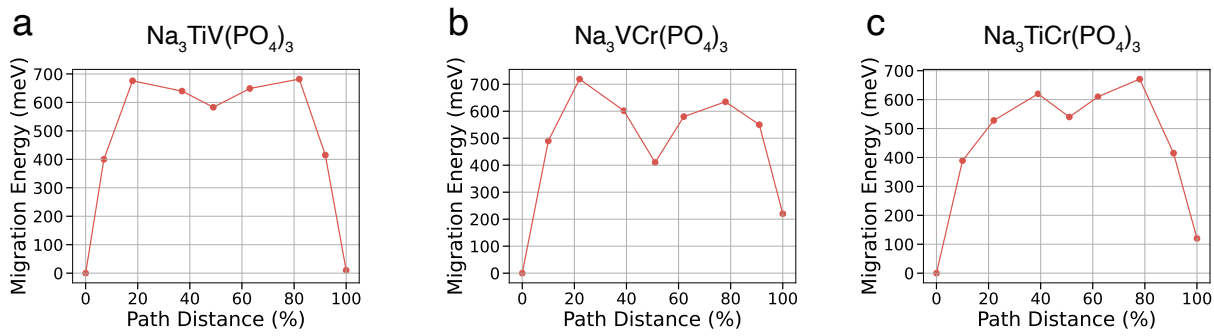


Figure S12: The computed minimum energy path of $\text{Na}_3\text{TiV}(\text{PO}_4)_3$ (panel a), $\text{Na}_3\text{VCr}(\text{PO}_4)_3$ (panel b), and $\text{Na}_3\text{TiCr}(\text{PO}_4)_3$ (panel c) by NEB with SCAN + U framework.

2 Local Cluster Expansion Formalism

A Local Cluster Expansion (LCE) model was applied to generate the Hamiltonian to rapidly reproduce the first-principles E_{KRA} and ΔE_{site} based on the local Na-vacancy (Va) sublattices within the migration unit (m.u.), see **Table S4**, which was constructed with a 4 Å cut-off to search for the nearest-neighbor Na sites around Na(1).

Table S4: Cartesian coordinates (Å) for all the local Na/Va sites within the migration unit of $Na_xV_2(PO_4)_3$.

Na/Va Site Index	x	y	z
0	-3.086672	-0.829950	0.947705
1	-0.925527	3.110426	0.762916
2	-0.855745	0.829901	-3.113450
3	0.855685	-0.829963	3.113255
4	0.925471	-3.110625	-0.762970
5	3.086499	0.829901	-0.947748

Within the migration unit, pairs and triplets clusters were searched by cut-offs of 8 Å and 6 Å, respectively, resulting in totally 6 inequivalent orbitals. The information of all generated orbitals is summarized in **Table S5**.

Table S5: The truncated point, pair, and triplet interaction orbitals with the cut-offs of 8 Å and 6 Å for pairs and triplets respectively to generate the LCE formalism for $Na_xV_2(PO_4)_3$. The Site Index illustrates the representative indices for each orbital, and all the indices in the column Site Index are corresponding to the Na/Va Site Index in **Table S4**.

Index	Site Index	Type	Min_length	Max_length	Multiplicity
0	(0,)	point	0	0	6
1	(0, 1)	pair	4.498	4.498	6
2	(0, 2)	pair	4.922	4.922	6
3	(0, 5)	pair	6.668	6.668	3
4	(0, 1, 2)	triplet	4.498	4.922	6
5	(0, 2, 4)	triplet	4.922	4.922	2

The LCE Hamiltonian to predict the E_{KRA} and ΔE_{site} can be written as

$$E = \sum_{\omega} K_{\omega} \phi_{\omega} + K_0 \quad (1)$$

where ω is the index for all the orbitals, ϕ_ω is the orbital function of ω incorporating all the interaction clusters within ω , and K_ω and K_0 are the Kinetic Effective Cluster Interaction (KECI) and empty cluster interaction coefficients to be determined. Specifically, the orbital function ϕ_ω is expanded as

$$\phi_\omega = \sum_{\delta \in \omega} \psi_\delta = \sum_{\delta \in \omega} \prod_{id \in \delta} \sigma_{id} \quad (2)$$

where ψ_δ is the cluster function of δ , which denotes all the equivalent clusters within the orbital ω , and id specifies the Na site occupation index of cluster δ . We assign $\sigma_{id} = -1$ for Na-occupied sites, and $\sigma_{id} = +1$ for Na-vacant sites, using the *Chebyshev* basis.

E_{KRA} and ΔE_{site} were fitted separately using Lasso fitting formalism with L1 norm, and thus 2 sets of KECI and empty cluster interactions were generated. In both of the fitting procedures of N_xVP systems, 5 non-zero KECI were identified as in **Tables S6 & S7**, and root-mean-square error (RMS) and leave-one-out cross-validation (LOOCV) were used to estimate the predictive accuracy of the LCE models as in **Figure S13**.

Table S6: Non-zero KECI (meV/multiplicity) as generated from LCE of N_xVP for E_{KRA} . The cluster indexes are corresponding to **Table S5**

Index	Cluster Index	Type	KECI
0	0	point	9.88
1	2	pair	14.53
2	3	pair	5.64
3	4	triplet	0.71
4	5	triplet	-32.61
5	Empty Cluster	-	328.26

Table S7: Non-zero KECI (meV/multiplicity) as generated from LCE of N_xVP for ΔE_{site} . The cluster indexes are corresponding to **Table S5**

Index	Cluster Index	Type	KECI
0	0	point	48.48
1	1	pair	1.58
2	2	pair	19.61
3	3	pair	28.04
4	4	triplet	-7.22
5	Empty Cluster	-	280.75

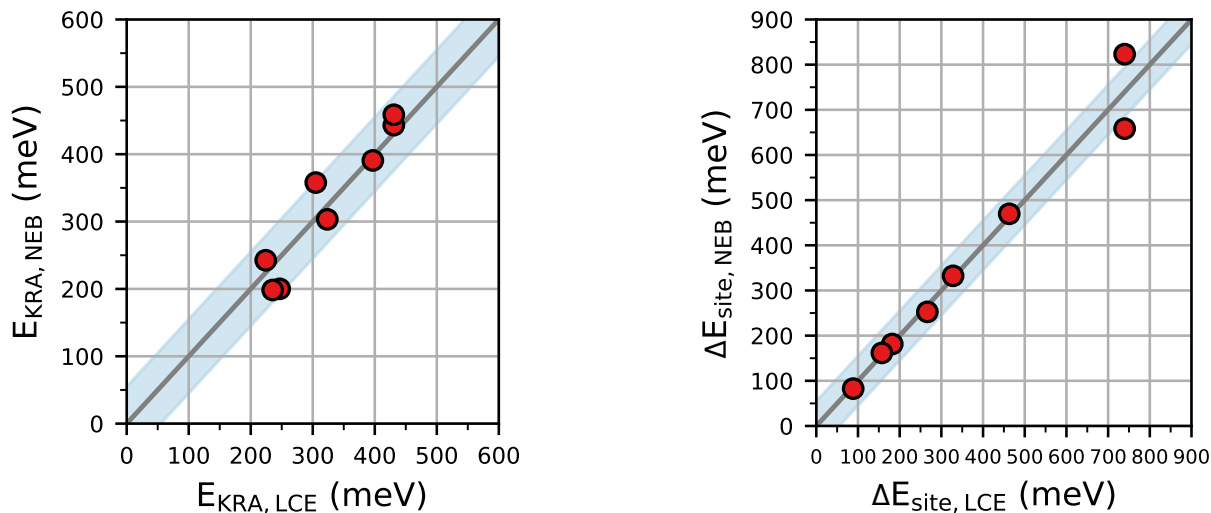


Figure S13: DFT and LCE predicted E_{KRA} and ΔE_{site} for N_xVP . The RMS were ± 31.75 meV and ± 41.71 meV for E_{KRA} and E_{site} , respectively.

The structural motif and LCE fitting results of N_xCP , and N_xTP are summarized in **Tables S8 ~ S11 & Figure S14**, and **Tables S12 ~ S15 & Figure S15**, respectively.

Table S8: Cartesian coordinates (\AA) for all the local Na/Va sites within the migration unit of $Na_xCr_2(PO_4)_3$.

Na/Va Site Index	x	y	z
0	-3.077470	-0.808393	0.819679
1	-0.851576	3.065802	-0.819679
2	-0.765049	-0.862416	-3.076870
3	0.765050	0.862417	3.076870
4	0.851576	-3.065802	0.819679
5	3.077470	0.808393	-0.819679

Table S9: The truncated point, pair, and triplet interaction orbitals with the cut-offs of 8 Å and 6 Å for pairs and triplets respectively to generate the LCE formalism for $\text{Na}_x\text{Cr}_2(\text{PO}_4)_3$. The Site Index illustrates the representative indices for each orbital, and all the indices in the column Site Index are corresponding to the Na/Va Site Index in **Table S8**.

Index	Site Index	Type	Min_length	Max_length	Multiplicity
0	(0,)	point	0	0	6
1	(0, 1)	pair	4.759	4.759	6
2	(0, 2)	pair	4.531	4.531	6
3	(0, 5)	pair	6.572	6.572	3
4	(0, 1, 2)	triplet	4.759	4.531	6
5	(0, 2, 4)	triplet	4.759	4.759	2

Table S10: Non-zero KECI (meV/multiplicity) as generated from LCE of N_xCP for E_{KRA} . The cluster indexes are corresponding to **Table S9**

Index	Cluster Index	Type	KECI
0	1	pair	10.73
1	2	pair	15.01
2	3	pair	6.39
3	4	triplet	1.83
4	5	triplet	-4.54
5	Empty Cluster	-	348.90

Table S11: Non-zero KECI (meV/multiplicity) as generated from LCE of N_xCP for ΔE_{site} . The cluster indexes are corresponding to **Table S9**

Index	Cluster Index	Type	KECI
0	0	point	68.13
1	1	pair	-1.89
2	2	pair	17.60
3	3	triplet	10.88
4	5	triplet	-44.73
5	Empty Cluster	-	403.21

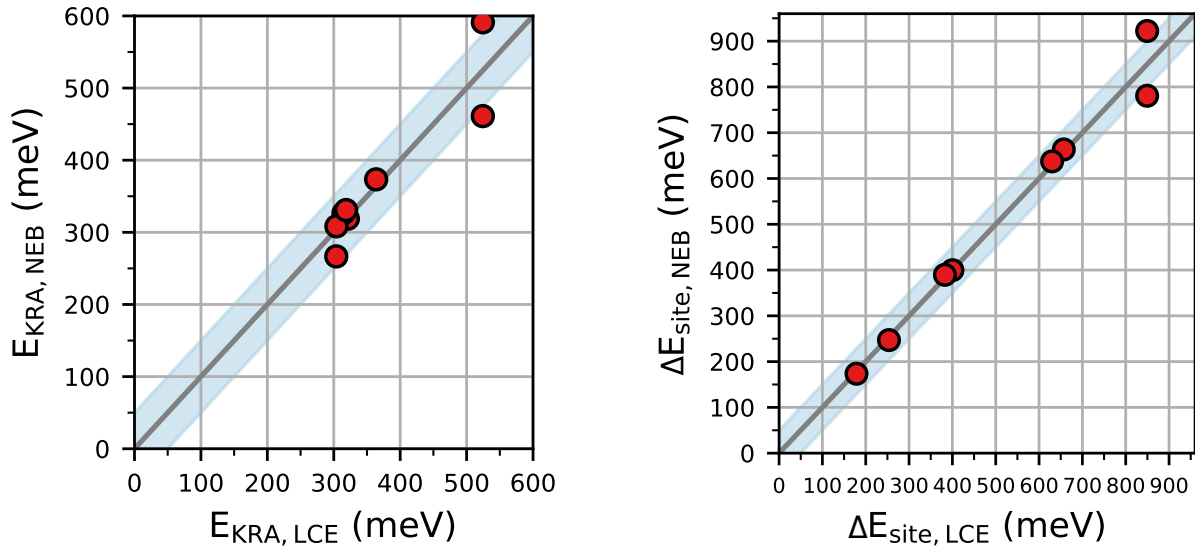


Figure S14: DFT and LCE predicted E_{KRA} and ΔE_{site} for N_xCP . The RMS were ± 35.81 meV and ± 35.76 meV for E_{KRA} and E_{site} , respectively.

Table S12: Cartesian coordinates (\AA) for all the local Na/Va sites within the migration unit of $\text{Na}_x\text{Ti}_2(\text{PO}_4)_3$.

Na/Va Site Index	x	y	z
0	-3.163969	-0.940097	0.916997
1	-1.016608	3.140221	0.916997
2	-0.863031	0.995955	-3.162058
3	0.863031	-0.995956	3.162058
4	1.016608	-3.140221	-0.916997
5	3.163969	0.940096	-0.916997

Table S13: The truncated point, pair, and triplet interaction orbitals with the cut-offs of 8 \AA and 6 \AA for pairs and triplets respectively to generate the LCE formalism for $\text{Na}_x\text{Ti}_2(\text{PO}_4)_3$. The Site Index illustrates the representative indices for each orbital, and all the indices in the column Site Index are corresponding to the Na/Va Site Index in **Table S12**.

Index	Site Index	Type	Min_length	Max_length	Multiplicity
0	(0,)	point	0	0	6
1	(0, 1)	pair	4.611	4.611	6
2	(0, 2)	pair	5.068	5.068	6
3	(0, 5)	pair	6.851	6.851	3
4	(0, 1, 2)	triplet	5.068	4.611	6
5	(0, 2, 4)	triplet	5.068	5.068	2

Table S14: Non-zero KECI (meV/multiplicity) as generated from LCE of N_xTP for E_{KRA} . The cluster indexes are corresponding to **Table S13**

Index	Cluster Index	Type	KECI
0	0	point	0.66
1	1	pair	13.87
2	3	pair	-3.14
3	4	triplet	0.40
4	5	triplet	-6.32
5	Empty Cluster	-	284.70

Table S15: Non-zero KECI (meV/multiplicity) as generated from LCE of N_xTP for ΔE_{site} . The cluster indexes are corresponding to **Table S13**

Index	Cluster Index	Type	KECI
0	0	point	34.52
1	1	pair	49.36
2	3	pair	-35.29
3	4	triplet	-8.79
4	5	triplet	-48.05
5	Empty Cluster	-	418.819204

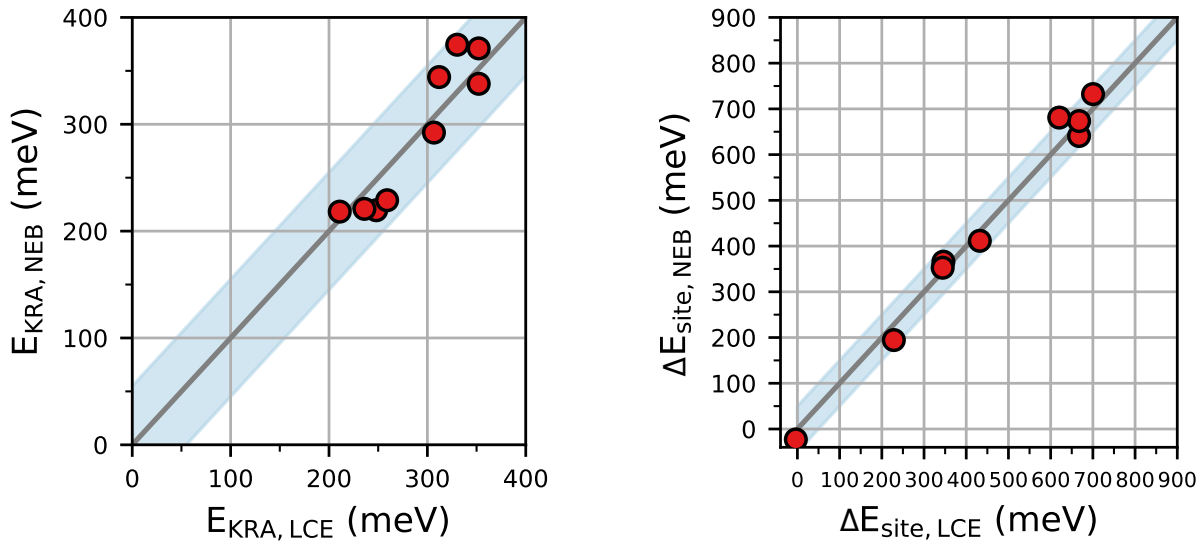


Figure S15: DFT and LCE predicted E_{KRA} and ΔE_{site} for N_xTP . The RMS were ± 25.29 meV and ± 29.56 meV for E_{KRA} and E_{site} , respectively.

The Na^+ diffusion barrier energy ($E_{barrier}$) can be computed for the next-step kinetic Monte Carlo Simulation, with the LCE-generated ΔE_{site} and E_{KRA} using **equation (3)**:

$$E_{barrier} = \frac{\sigma_2 - \sigma_1}{4} \Delta E_{site} + E_{KRA} \quad (3)$$

where σ_2 and σ_1 are the site occupations of Na(2) and Na(1) sites, respectively.

3 Kinetic Monte Carlo Simulations

Using the as-generated LCE Hamiltonian in **Section 2**, we sampled all possible stochastic Na^+ hop events within the $\text{Na}_x\text{M}_2(\text{PO}_4)_3$ intercalation systems, through the kinetic Monte Carlo (kMC) method as reported by Anton van der Ven et al.^{S17,S18}

The migration barrier energy (E_{barrier}) for an individual hop event can be calculated using **Eq. (3)**, and the corresponding migration probability can be evaluated as

$$\Gamma_{\text{event}} = \nu^* \exp\left(\frac{-E_{\text{barrier}}}{k_B T}\right) \quad (4)$$

where the prefactor ν^* related to the activation entropy along diffusion pathways is assumed to be 1×10^{13} Hz in this work, k_B is the *Boltzmann* constant and T is the temperature for the kMC simulation.

All possible migration probabilities can be evaluated using **Eq. (4)**, and subsequently, the specific hop event k was chosen by a random number ρ ($\rho \in (0, 1)$) such that

$$\frac{1}{\Gamma_{\text{tot}}} \sum_{i=1}^{k-1} \Gamma_i < \rho \leq \frac{1}{\Gamma_{\text{tot}}} \sum_{i=1}^k \Gamma_i \quad (5)$$

where Γ_{tot} is the summation of all individual migration probabilities. The diffusion time (Δt) of the chose event k was estimated with a random number ϵ between 0 and 1 using **Eq. (6)**:

$$\Delta t = \frac{-\ln(\epsilon)}{\Gamma_{\text{tot}}} \quad (6)$$

Each kMC simulation for $\text{Na}_x\text{V}_2(\text{PO}_4)_3$ systems was initialized from the supercell configuration with $8 \times 8 \times 8$ f.u. at 973 K using the Canonical Monte Carlo (CMC) model from Wang et al.,^{S10} and was equilibrated between 4096000 and 40960000 steps. Notice that we didn't observe significant difference between the kMC results initialized from structures generated at high-temperature region with solid-solution behaviors, i.e., at 973 K (**Figure S21**),

or low-temperature region with clear phase-separation regions, i.e., at 300 K (**Figure S22**).

Specifically, only Na-vacancy sublattices were considered in this study, and P, V, O atoms were neglected. 37 compositions ($x = 1, 1.06, 1.125, 1.2, 1.25, 1.33, 1.375, 1.5, 1.625, 1.75, 1.875, 1.9, 2, 2.11, 2.125, 2.14, 2.16, 2.25, 2.375, 2.5, 2.625, 2.75, 2.84, 2.875, 2.9, 3, 3.05, 3.07, 3.1, 3.15, 3.2, 3.25, 3.3, 3.5, 3.625, 3.75, 3.875$) in total were computed from 300 K to 900 K by kMC, and 50 initial structures were incorporated as generated by CMC at each composition. All tracktable kMC-derived properties were statistically averaged at each composition and each temperature.

Na^+ tracer diffusivity (D^*), jump diffusivity (D_J) were tracked while Na^+ hopping during kMC simulations and were arithmetically averaged. The tracer diffusivity was given by **Eq. (7)**:

$$D^* = \frac{1}{6tN} \sum_{m=1}^N (\overrightarrow{r_m(t)})^2 \quad (7)$$

and the jump diffusivity was given by **Eq. (8)**:

$$D_J = \frac{1}{6tN} \left(\sum_{m=1}^N \overrightarrow{r_m(t)} \right)^2 \quad (8)$$

where $\overrightarrow{r_m(t)}$ is the tracked ion-displacement of Na^+ m after diffusion time t, and N denotes the total number of hopping Na-ions within the supercell. Note that, for $\text{Na}_x\text{V}_2(\text{PO}_4)_3$ system at 300 K, we derive a polynomial fit of the 4th order $D_J(x) = -10.36 - 18.88x + 22.08x^2 - 8.479x^3 + 1.086x^4$ to reflect the physical origins of the variation in D_J which depend on Na-Vacancy configurations (see main article).

The overall D_J can be separated by the contributions from Na(1), and Na(2) ions using **Eq. (9)** and **Eq. (10)**:

$$D_J \text{Na}(1) = \frac{1}{6tN_1} \left(\sum_{m=1}^{N_1} \overrightarrow{r_{m1}(t)} \right)^2 \quad (9)$$

$$D_J \text{Na}(2) = \frac{1}{6tN_2} \left(\sum_{m=1}^{N_2} \overrightarrow{r_{m2}(t)} \right)^2 \quad (10)$$

where N_1 , and N_2 are the number of hopping Na(1), and Na(2) ions, respectively. $\overrightarrow{r_{m1}(t)}$, and $\overrightarrow{r_{m2}(t)}$ were the displacement of Na(1), and Na(2) after diffusion time t.

Using a Nernst-Einstein approximation, our diffusion can be transformed into ionic conductivities σ , using **Eq. (11)**:

$$\sigma = \frac{e^2 C}{k_B T} D_J \quad (11)$$

where e is the electron charge, C is the volumetric concentration of diffusion Na-ions, and D_J is the jump diffusivity given by **Eq. (8)**. In the case of $\text{Na}_x\text{V}_2(\text{PO}_4)_3$, at 300 K, values of σ appear to reach a maximum at intermediate compositions near $x = 3$ ($\sim 2 \times 10^{-2}$ S/cm).

D_J can be further used to calculate the chemical diffusion coefficient (D_C) with **Eq. (12)**:

$$D_C = \Theta D_J \quad (12)$$

where the thermodynamic factor Θ can be estimated from the grand canonical Monte Carlo work of Wang et al.^{S10} using **Eq. (13)**:

$$\Theta = \frac{\partial \frac{\mu}{k_B T}}{\partial x} \quad (13)$$

where μ is the chemical potential of migrating Na-ion at the composition x . The computed Θ at different temperature regions were shown in **Figure S16**. **Figure S16a** corresponds to Θ as derived from the 3 single phase domains at 300 K, whereas the high-T Θ results as shown in **Figure S16b** agrees with the solid-solution behavior of $\text{Na}_x\text{V}_2(\text{PO}_4)_3$ at ~ 900 K.

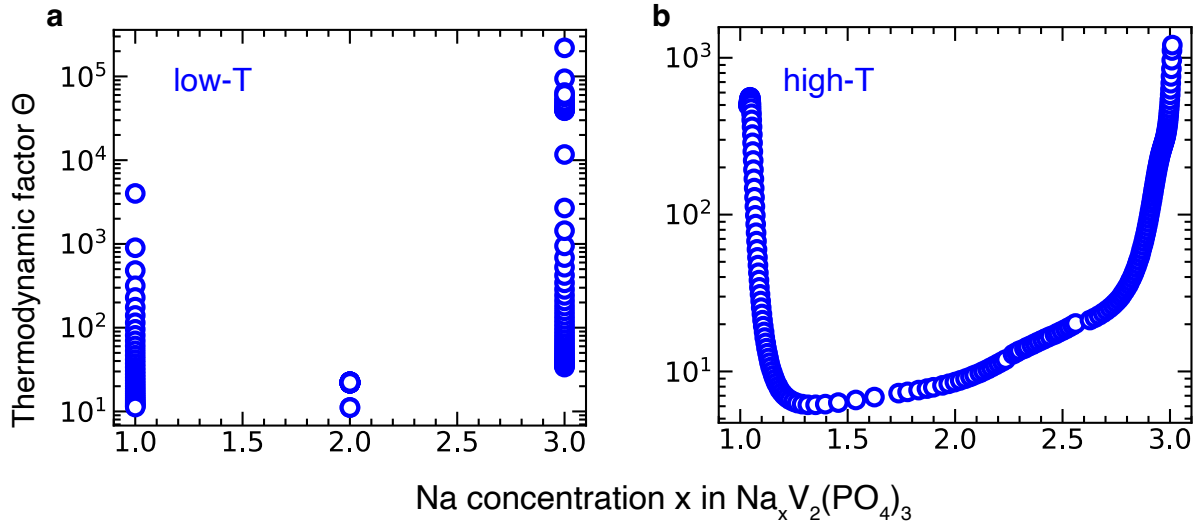


Figure S16: The computed thermodynamic factor Θ at different temperature (T) regions derived from the grand canonical Monte Carlo simulations of our prior work.^{S10} Panel **a** shows the Θ derived at low- T , i.e., ~ 300 K at room temperature, and panel **b** depicts the Θ at high- T , i.e., ~ 900 K.

The computed chemical diffusivity coefficients of $\text{Na}_x\text{V}_2(\text{PO}_4)_3$ systems at the most applicable composition ($x = 1 \sim 3$) was shown in **Figure S17**. *Vegard's law* was applied to refine the chemical diffusivity coefficients such that only the data points of single-phase region are shown, while the kMC results residing in the biphasic regions are replaced by the dashed lines connecting the end members at the phase boundaries.

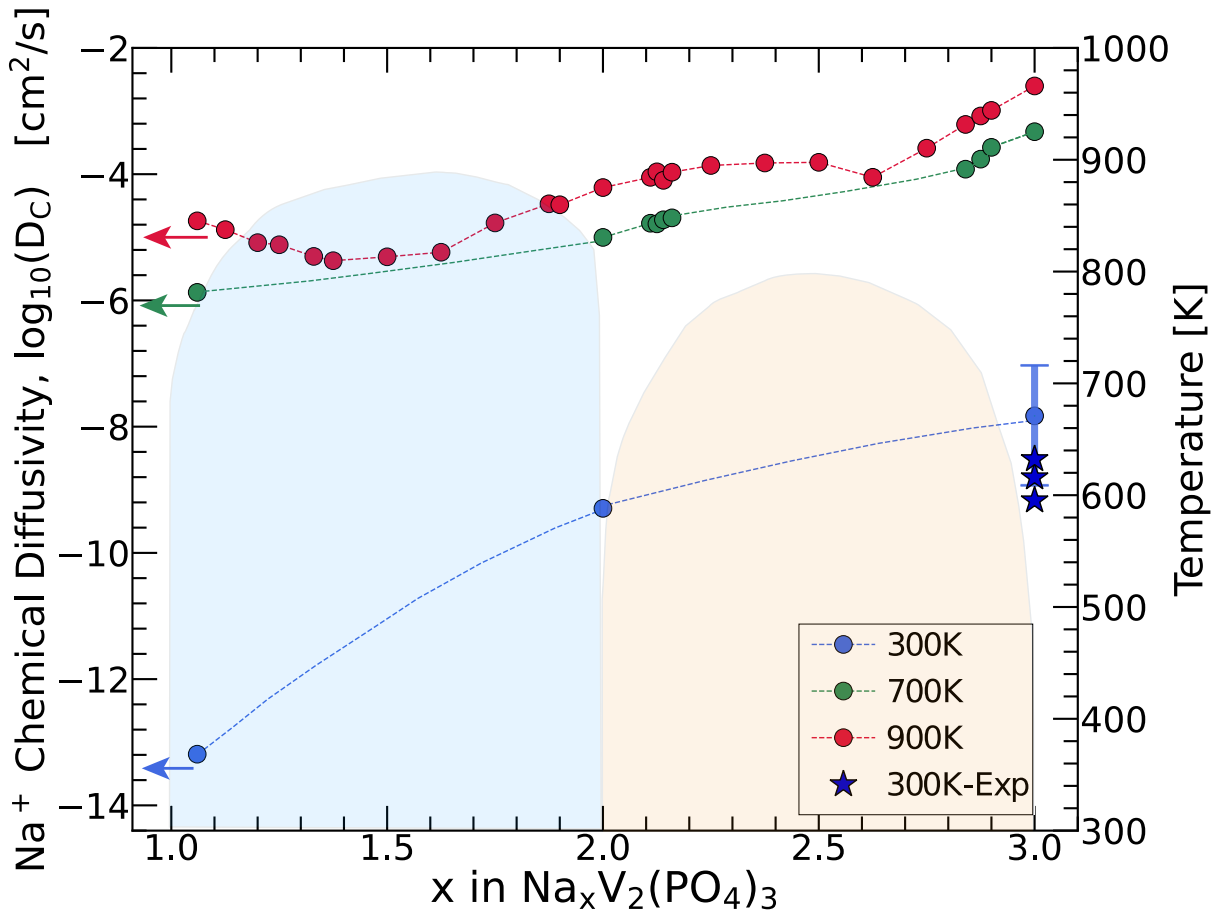


Figure S17: The computed chemical diffusivity coefficients of $\text{Na}_x\text{V}_2(\text{PO}_4)_3$ at 300K ((blue), 700K (green), and 900k (red)). The error bar at $x = 3$ at 300K illustrates our computational confidence interval. The phase diagram are adapted from our previous work.^{S10}

The calculated charge carrier concentration of $\text{Na}_x\text{V}_2(\text{PO}_4)_3$ system at 300 K was depicted in **Figure S18**. To be noted, similar diffusion carrier profiles of $\text{Na}_x\text{Ti}_2(\text{PO}_4)_3$ and $\text{Na}_x\text{Cr}_2(\text{PO}_4)_3$ systems were observed.

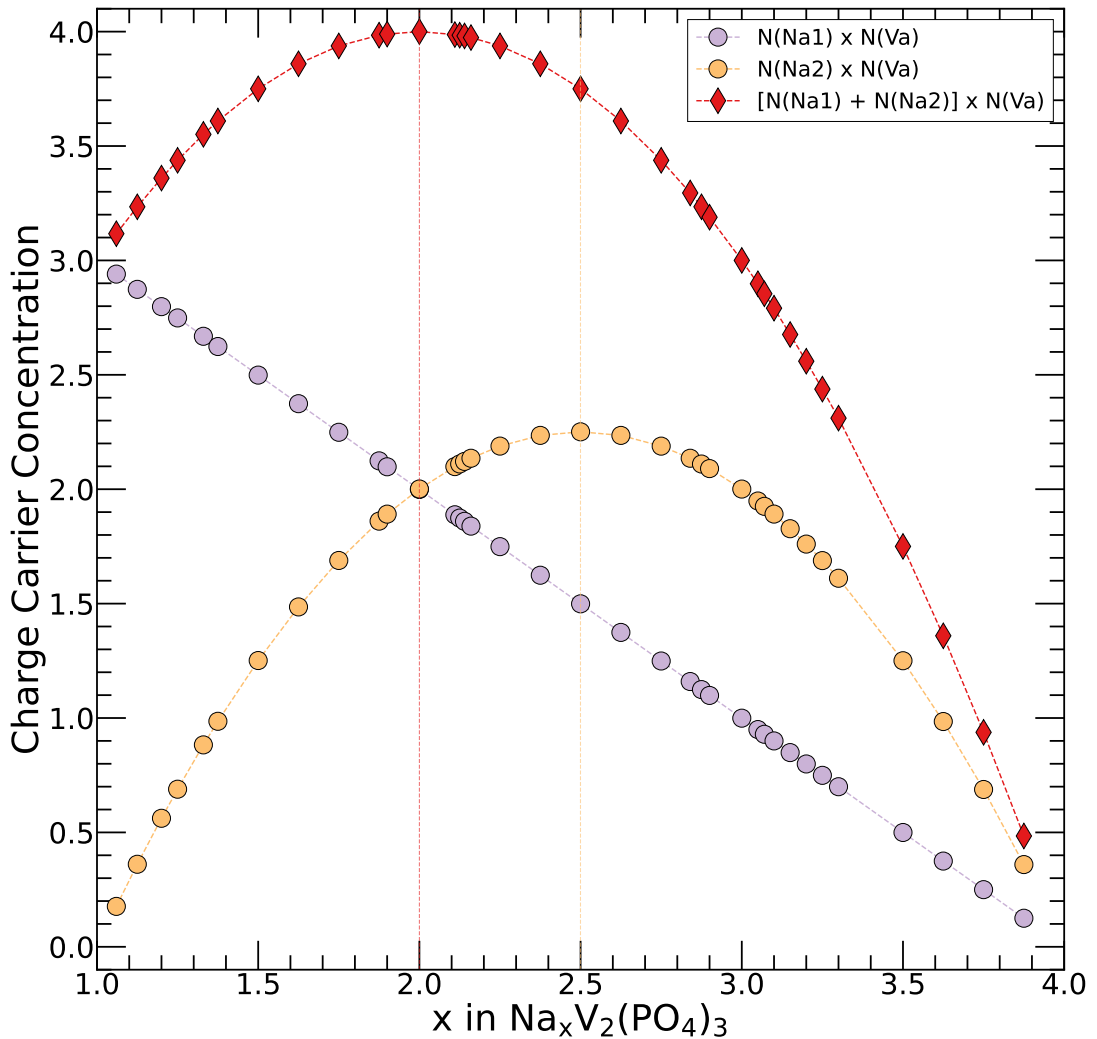


Figure S18: The computed charge carrier concentrations of $\text{Na}_x\text{V}_2(\text{PO}_4)_3$ at 300 K. The number of Na(1), Na(2), and vacancy per formula unit were denoted by $N(\text{Na1})$, $N(\text{Na2})$, and $N(\text{Va})$, respectively. The $N(\text{Na1}) \times N(\text{Va})$ (purple), $N(\text{Na2}) \times N(\text{Va})$ (yellow), and $[N(\text{Na1}) + N(\text{Na2})] \times N(\text{Va})$ (red) as a function of Na composition were used to evaluate the corresponding diffusion charge carrier concentrations, contributed from the population of Na(1), Na(2), and the overall Na^+ . The Na compositions giving rise to the maximum $N(\text{Na2}) \times N(\text{Va})$, and $[N(\text{Na1}) + N(\text{Na2})] \times N(\text{Va})$ values were shown with the vertical yellow line, and red line, respectively.

The fractional vacancy occupancy of Na(1), and Na(2) sites are shown in **Figure S19**.

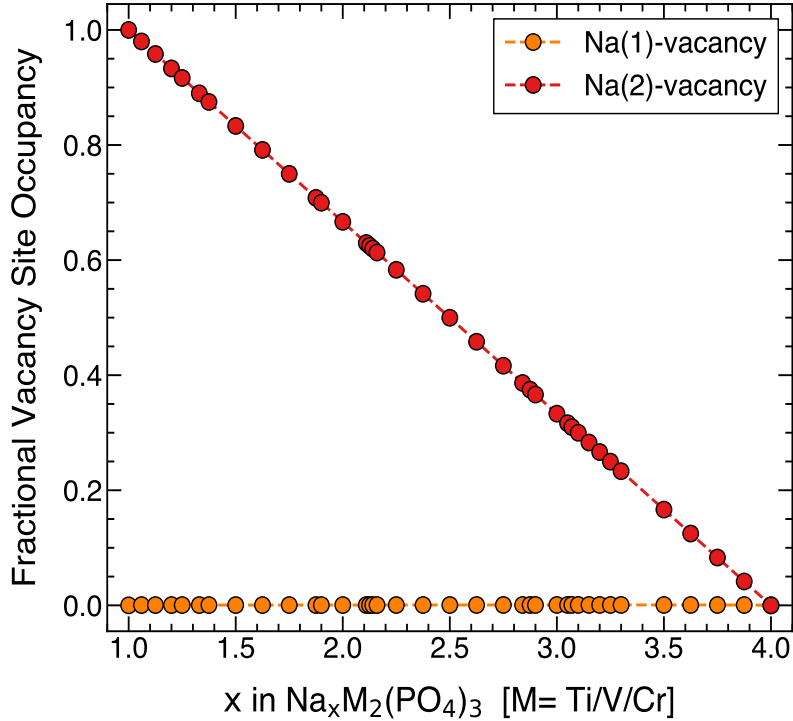


Figure S19: Fractional vacancy occupancy at 300 K of Na(1) and Na(2) sites in $\text{Na}_x\text{M}_2(\text{PO}_4)_3$ ($\text{M} = \text{Ti}, \text{V}, \text{or Cr}$), which corresponds to the inverse value of Figure 3 in the main article. The computed vacancy-site occupancies do not show significant differences within our kMC simulations, hence data for $\text{Na}_x\text{V}_2(\text{PO}_4)_3$ is plotted.

For $\text{Na}_x\text{Cr}_2(\text{PO}_4)_3$ and $\text{Na}_x\text{Ti}_2(\text{PO}_4)_3$ systems, we started from the same initial Na-vacancy sublattices as implemented in $\text{Na}_x\text{V}_2(\text{PO}_4)_3$ (generated using CMC at 973 K), and simulated following the kMC procedures as described above at the same compositional and temperature regions.

The calculated tracer diffusion coefficients (D^*), jump diffusion coefficients (D_J), and conductivity (σ), which were normalized by a factor of $10^{13}/\nu^*$, for all $\text{Na}_x\text{Ti}_2(\text{PO}_4)_3$, $\text{Na}_x\text{V}_2(\text{PO}_4)_3$, and $\text{Na}_x\text{Cr}_2(\text{PO}_4)_3$ systems from 300 K to 800 K, as a function of Na composition were shown in **Figures S20 ~ S23**.

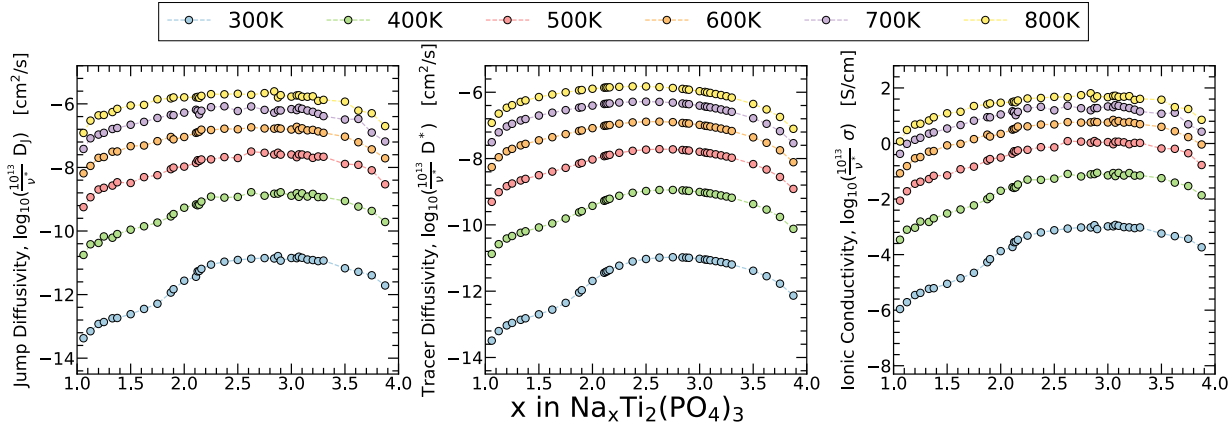


Figure S20: The computed tracer diffusion coefficients (D^*), jump diffusion coefficients (D_J), and conductivity (σ) for $\text{Na}_x\text{Ti}_2(\text{PO}_4)_3$ system from 300 K to 800 K. The results were obtained by our KMC simulations, and normalized by a factor of $10^{13}/\nu^*$.

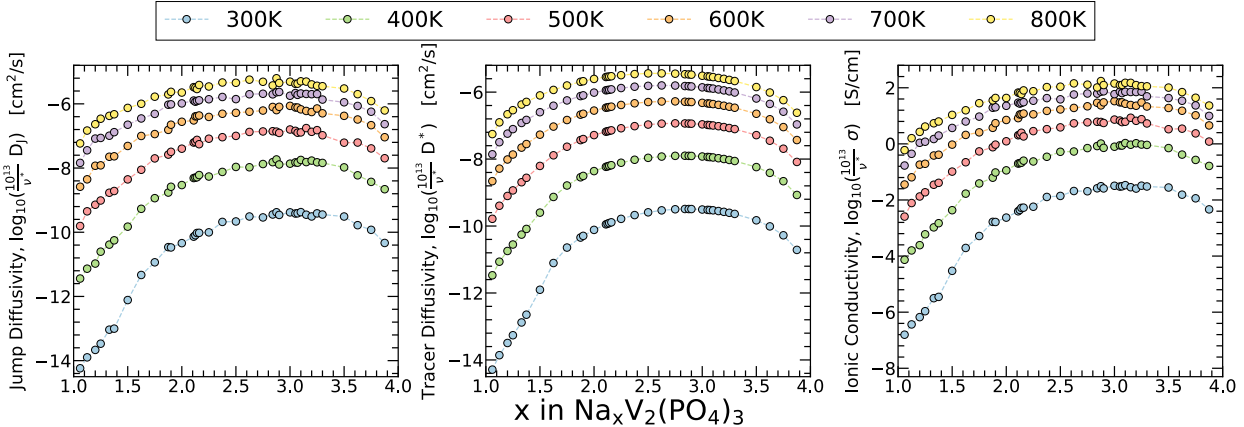


Figure S21: The computed tracer diffusion coefficients (D^*), jump diffusion coefficients (D_J), and conductivity (σ) for $\text{Na}_x\text{V}_2(\text{PO}_4)_3$ system from 300 K to 800 K. The results were obtained by our KMC simulations, and normalized by a factor of $10^{13}/\nu^*$. The results were derived from the structures initialized using Canonical Monte Carlo simulations at 973 K.

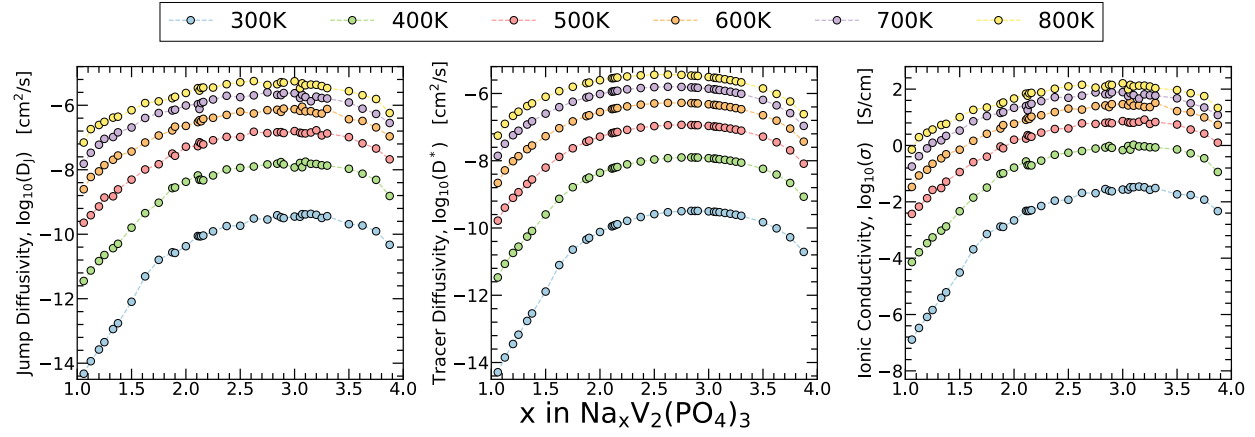


Figure S22: The computed tracer diffusion coefficients (D^*), jump diffusion coefficients (D_J), and conductivity (σ) for $\text{Na}_x\text{V}_2(\text{PO}_4)_3$ system from 300 K to 800 K. The results were obtained by our KMC simulations, and normalized by a factor of $10^{13}/\nu^*$. The results were derived from the structures initialized using Canonical Monte Carlo simulations at 300 K.

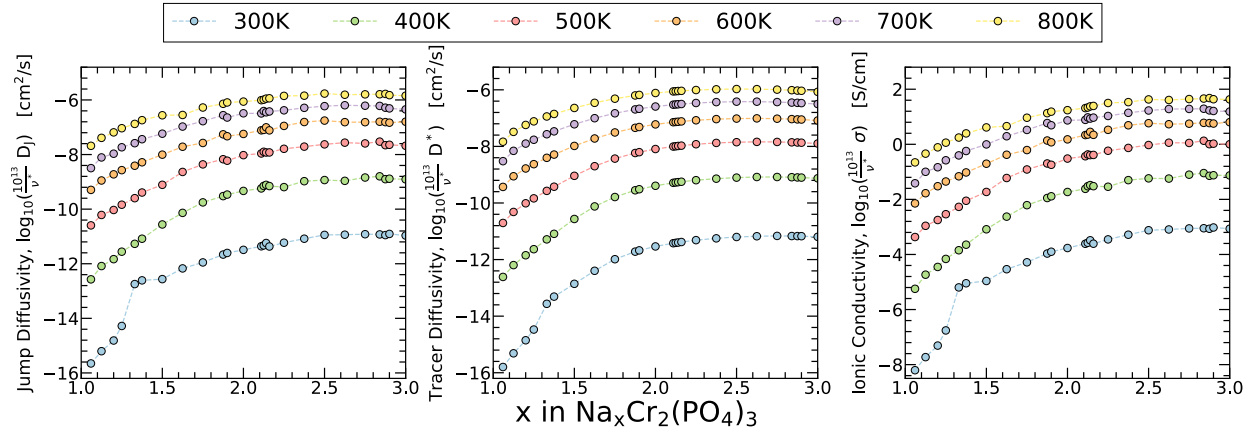


Figure S23: The computed tracer diffusion coefficients (D^*), jump diffusion coefficients (D_J), and conductivity (σ) for $\text{Na}_x\text{Cr}_2(\text{PO}_4)_3$ system from 300 K to 800 K. The KMC results were obtained from the LCE formalism fitted to the Na composition region of $x = 1$ to $x = 3$, and normalized by a factor of $10^{13}/\nu^*$.

References

- (S1) Kresse, G.; Furthmüller, J. Efficiency of ab-initio total energy calculations for metals and semiconductors using a plane-wave basis set. *Computational Materials Science* **1996**, *6*, 15–50.
- (S2) Kresse, G.; Furthmüller, J. Efficient iterative schemes for *ab initio* total-energy calculations using a plane-wave basis set. *Physical Review B* **1996**, *54*, 11169–11186.
- (S3) Kresse, G.; Joubert, D. From ultrasoft pseudopotentials to the projector augmented-wave method. *Physical Review B* **1999**, *59*, 1758–1775.
- (S4) Sun, J.; Ruzsinszky, A.; Perdew, J. Strongly Constrained and Appropriately Normed Semilocal Density Functional. *Physical Review Letters* **2015**, *115*, 036402.
- (S5) Long, O. Y.; Sai Gautam, G.; Carter, E. A. Evaluating optimal U for 3 d transition-metal oxides within the SCAN+ U framework. *Physical Review Materials* **2020**, *4*, 045401.
- (S6) Devi, R.; Singh, B.; Canepa, P.; Sai Gautam, G. Effect of exchange-correlation functionals on the estimation of migration barriers in battery materials. *npj Computational Materials* **2022**, *8*, 160.
- (S7) Sai Gautam, G.; Carter, E. A. Evaluating transition metal oxides within DFT-SCAN and SCAN + U frameworks for solar thermochemical applications. *Physical Review Materials* **2018**, *2*, 095401.
- (S8) Sheppard, D.; Xiao, P.; Chemelewski, W.; Johnson, D. D.; Henkelman, G. A generalized solid-state nudged elastic band method. *The Journal of Chemical Physics* **2012**, *136*, 074103.
- (S9) Sheppard, D.; Terrell, R.; Henkelman, G. Optimization methods for finding minimum energy paths. *The Journal of Chemical Physics* **2008**, *128*, 134106.

- (S10) Wang, Z.; Park, S.; Deng, Z.; Carlier, D.; Chotard, J.-N.; Croguennec, L.; Gautam, G. S.; Cheetham, A. K.; Masquelier, C.; Canepa, P. Phase stability and sodium-vacancy orderings in a Na₃V₂(PO₄)₃ electrode. *Journal of Materials Chemistry A* **2022**, *10*, 209–217.
- (S11) Park, S.; Wang, Z.; Deng, Z.; Moog, I.; Canepa, P.; Fauth, F.; Carlier, D.; Croguennec, L.; Masquelier, C.; Chotard, J.-N. Crystal Structure of Na₂V₂(PO₄)₃, an Intriguing Phase Spotted in the Na₃V₂(PO₄)₃–Na₁V₂(PO₄)₃ System. *Chemistry of Materials* **2022**, *34*, 451–462.
- (S12) Singh, B.; Wang, Z.; Park, S.; Gautam, G. S.; Chotard, J.-N.; Croguennec, L.; Carlier, D.; Cheetham, A. K.; Masquelier, C.; Canepa, P. A chemical map of Na₃V₂(PO₄)₃ electrode materials for sodium-ion batteries. *Journal of Materials Chemistry A* **2021**, *9*, 281–292.
- (S13) Chotard, J.-N.; Rousse, G.; David, R.; Mentré, O.; Courty, M.; Masquelier, C. Discovery of a Sodium-Ordered Form of Na₃V₂(PO₄)₃ below Ambient Temperature. *Chemistry of Materials* **2015**, *27*, 5982–5987.
- (S14) Nogai, A. S.; Stefanovich, S. Y.; Bush, A. A.; Uskenbaev, D. E.; Nogai, A. A. Dipole ordering and ionic conductivity in NASICON-Type Na₃Cr₂(PO₄)₃ structures. *Physics of the Solid State* **2018**, *60*, 23–30.
- (S15) Kawai, K.; Zhao, W.; Nishimura, S.-i.; Yamada, A. High-Voltage Cr⁴⁺/Cr³⁺ Redox Couple in Polyanion Compounds. *ACS Applied Energy Materials* **2018**, *1*, 928–931.
- (S16) Senguttuvan, P.; Rousse, G.; Arroyo y de Dompablo, M. E.; Vezin, H.; Tarascon, J.-M.; Palacín, M. R. Low-Potential Sodium Insertion in a NASICON-Type Structure through the Ti(III)/Ti(II) Redox Couple. *Journal of the American Chemical Society* **2013**, *135*, 3897–3903.

- (S17) Van der Ven, A.; Ceder, G.; Asta, M.; Tepesch, P. D. First-principles theory of ionic diffusion with nondilute carriers. *Physical Review B* **2001**, *64*, 184307.
- (S18) Van der Ven, A.; Thomas, J. C.; Xu, Q.; Swoboda, B.; Morgan, D. Nondilute diffusion from first principles: Li diffusion in Li_xTiS₂. *Physical Review B* **2008**, *78*, 104306.